Published in Annals of Biomedical Engineering
Full reference: Yeoman MS, Reddy BD, Bowles H, Bezuidenhout D, Zilla P, Franz T. The use of finite element methods and genetic algorithms in search of an optimal fabric reinforced porous graft system. Ann Biomed Eng, 2009, 37(11), 2266-87

The Use of Finite Element Methods and Genetic Algorithms in Search of an Optimal Fabric Reinforced Porous Graft System

M.S. Yeoman[a,c], B.D. Reddy[a], H.C. Bowles[b], P. Zilla[c], D. Bezuidenhout[c], T. Franz[c,*]

[a] *Centre for Research in Computational and Applied Mechanics, University of Cape Town, Rondebosch, South Africa*

[b] *Finite Element Analysis Services, Cape Town, South Africa*

[c] *Cardiovascular Research Unit, Chris Barnard Department of Cardiothoracic Surgery, University of Cape Town, Observatory, South Africa*

Short Title: FEM and GA for Search of Fabric Reinforced Porous Graft

***Correspondence address:**

Thomas Franz, PhD

Cardiovascular Research Unit

Faculty of Health Sciences

University of Cape Town

Private Bag X3

Observatory, 7935

South Africa

Tel: +27 21 406 6418

Fax: +27 21 448 5935

Email: thomas.franz@uct.ac.za

Abstract

The mechanics of arteries result from the properties of the soft tissue constituents and the interaction of the wall layers, predominantly media and adventitia. This concept was adopted in this study for the design of a tissue regenerative vascular graft. To achieve the desired structural properties of the graft, most importantly a diametric compliance of 6 %/100mmHg, finite element methods and genetic algorithms were used in an integrated approach to identify the mechanical properties of an adventitial fabric layer that were required to optimally complement an intimal/medial polyurethane layer with interconnected porosity of three different size classes. The models predicted a compliance of 16.0, 19.2, and 31.5 %/100mmHg for the non-reinforced grafts and 5.3, 5.5 and 6.0 %/100mmHg for the fabric-reinforced grafts. The latter, featuring fabrics manufactured according to the required non-linear mechanical characteristics numerically predicted, exhibited an in-vitro compliance of 2.1 ± 0.8, 3.0 ± 2.4 and 4.0 ± 0.7 %/100mmHg. The combination of finite element methods and genetic algorithms was shown to be able to successfully optimize the mechanical design of the composite graft. The method offers potential for the application to alternative concepts of modular vascular grafts and the incorporation of tissue ingrowth and biodegradation.

Keywords:

Adventitial reinforcement; Constitutive model; Diametric compliance; Numerical modeling; Optimization; Vascular mechanics; Vascular prosthesis

Contents

1 Introduction

Although the mechanisms behind sub-optimal patency and failure of small- to medium-diameter grafts are not fully understood, it is clear that compliance mismatch and the thrombogenetic nature of non-endothelialised surfaces are major contributors.[9,10,13,21,23,28,30] Previous studies have shown that it is a combination of the thrombogenetic nature of the graft material, surface roughness, and the mechanical and hemodynamic properties of the replacement graft in relation to the host artery which add up to the relatively poor performance of prosthetic grafts as compared with vein grafts or arterial grafts.[3,13]

Tissue engineering and regeneration efforts of the past two decades have aimed at the creation of biological interfaces between the blood and the prosthesis. As an alternative to the in-vitro endothelialization of conventional vascular prostheses with cultured autologous endothelial cells,[5] the concept of transmural endothelialization requires ingrowth-permissive graft structures.[12,13,16,30] Given the defined dimensions of capillaries and arterioles, many of the ill-defined porous structures investigated for this purpose exhibit pore interconnections which are too narrow to allow for complete penetration of the graft wall. Therefore, structures with well-defined interconnected micro-pores and channels have been developed with optimal porosities for both vascular ingrowth and mitigation of inflammation.[2] As much as the biological response patterns seem to require large, open porosity in thin-walled grafts, the resulting structural weakness and the excessive viscoelastic properties may pose a prohibitive obstacle.

Past research has utilized winding methods to reinforce these graft structures.[25] However, these methods cause radial compression, high stress concentrations, excessively reduced compliance and nonlinear effects in the region of the reinforcement.Thus, a better method of reinforcement is required which does not cause localized stress concentrations and hence excessive localized compression of the porous structure while still allowing for tissue regeneration through the support structure.

Fabric or mesh structures may offer advantages in externally reinforcing the porous polymer grafts more uniformly. However, complex mechanics impose a challenge for deriving optimal fabric designs that will, in combination with the porous structures, provide the desired mechanics of the reinforced grafts.

Genetic algorithms (GA) and finite element methods (FEM) have been used to study structural and thermal optimization problems in medicine. Khalil et al.[15] proposed a computational scheme for the elasticity reconstruction of soft tissue. The scheme comprises finite element modeling for mechanical analysis with genetic algorithms for parameter estimation, and was successfully applied to the elasticity characterization of atherosclerotic plaques in diseased arteries. A similar approach was followed by Hsu et al.[14] to optimize the design of locking screws used for fracture fixation and bone healing of tibial fractures. The two principal objectives in the design of these orthopedic screws are bending strength and bone holding power. Since these two objectives may conflict with each other, a multi-objective optimization method based on finite element modeling and genetic algorithms was used to evaluate and rank various screw designs.

Siauve et al.[22] showed a potential clinical utilization of genetic algorithms coupled with a finite element formulation. They developed a treatment tool for local hyperthermia treatment of cancer which optimizes radio-frequency and microwave sources so as to achieve a temperature distribution specific for individual patients.

The use of genetic algorithms has been successfully demonstrated for biomedical applications. Pandit et al.[20] and Wang et al.[27] utilized GAs for the development of a two-layer three-dimensional constitutive model for porcine coronary arteries. Approximating the arterial wall by an intima-media layer and an adventitial layer, they combined genetic algorithms with experimental testing to determine the material properties of each of the two layers. After testing intact arteries and their corresponding dissected adventitia or intima-media layer, the material properties of the missing layer were computed from the properties of the intact wall and the tested layer.

The aim of this work was to propose the use of an elastic knit fabric structure for the externally, i.e. 'adventitial', reinforcement of a porous polymeric vascular graft. The polymeric structure with well-defined interconnected porosity[1,2,4] served as scaffold for tissue integration and regeneration but exhibited low mechanical strength. The adventitial fabric acted as reinforcement for the porous scaffold, providing structural integrity and desired mechanical characteristics of the graft, while permitting cellular activity to take place through its structure. The design of the reinforcing fabric was facilitated with a combination of finite element methods and genetic algorithms. The process aimed at the determination of mechanical properties of the fabric structure that, combined with the porous polymeric structure, result in a specific dynamic compliance, nonlinear pressure-diameter response and diastolic diameter of the graft.

2 Materials and Methods

Two constitutive models, three finite element (FE) models and one genetic algorithm (GA) were employed in the body of the work. The constitutive models were used to describe the mechanics of the weak porous graft structure and the 'adventitial' fabric reinforcing. The FE models included one graft model and two fabric models. The graft model was utilized to describe the mechanics of the combined graft of porous graft structure and 'adventitial' fabric reinforcing. The fabric FE models for circumferential and longitudinal tension, respectively, were applied to describe the transverse mechanics, in warp and weft direction, of the fabric for both loading cases. The GA served to adjust the parameters of the fabric constitutive model utilized in the graft FE model in order to optimize the mechanical characteristics of the graft: dynamic compliance, nonlinear pressure-diameter response and diastolic diameter. The optimized parameters of the fabric constitutive model, obtained from the GA, were then utilized in the circumferential and longitudinal FE models to obtain transverse stress-strain curves for an ideal

'adventitial' fabric reinforcing. These transverse stress-strain curves were subsequently used to find feasible physical fabric structures.

2.1 Constitutive Modeling

2.1.1 Porous polymer graft structures

The porous grafts containing well-defined, interconnected pores used in this study were manufactured using biostable PUR, an ether-free aliphatic segmented polyurethane[26] and extractable highly regular spherical porogen (gelatin micro-spheres, Thies Technologies, St. Louis, MO, USA) of three different nominal size ranges of 90-106, 106-125, and 125-150 μm. On average, the pores created in the polyurethane structure were 1.21 ± 0.07 times the diameter of the porogen from which they were formed, while the interconnecting windows were 0.52 ± 0.04 times the diameter.[1]

In this study a hyperfoam strain energy function ψ[24] was used to describe the porous polymer:

$$\begin{aligned} \psi\left(\bar{\lambda}_1, \bar{\lambda}_2, \bar{\lambda}_3\right) &= \sum_{i=1}^{N} \frac{2\mu_i}{\alpha_i^2}\left[\left(\bar{\lambda}_1^{\alpha_i} + \bar{\lambda}_2^{\alpha_i} + \bar{\lambda}_3^{\alpha_i} - 3\right) + 3\left(J^{\frac{1}{3}\alpha_i} - 1\right)\right. \\ &\quad \left. + \frac{1}{\beta_i}\left(J^{-\alpha_i\beta_i} - 1\right)\right] . \end{aligned} \tag{1}$$

Here λ_k $(k = 1, 2, 3)$ are the principal stretches, J is the Jacobian of the deformation gradient and represents the ratio of current to initial volume change, $\overline{\lambda}_i = J^{1/3}\lambda_i$ are normalized stretches, and α_i, β_i, and μ_i are material constants.

The hyperfoam material model was validated through experimental tensile, compressive and shear tests. The tests were performed under physiological conditions on unit disk samples of the porous PUR of the various porogen size groups. The experimental and numerical data agreed well for tensile and compressive strain not exceeding 55 % and 30 %, respectively. Since the porous structures experience a maximum tensile strain

of about 30 % under physiological conditions, these limits were not deemed problematic.

2.1.2 Fabric reinforcing

We introduced a fabric strain energy function based on the exponential soft tissue model of Fung et al.[7] which was adapted to describe the general tensile characteristics of a coarse-knit fabric. The fabric was modeled as a compressible nonlinearly elastic thin membrane under conditions of plane stress. The strain energy function was given as a function of in-plane strains by

$$\begin{aligned} w(E_{ij}) &= \frac{C}{2}\exp\big[a_1(E_{11}^2)+a_2(E_{22}^2)+a_3(E_{12}^2+E_{21}^2)+a_4(E_{11}E_{22})+a_5(E_{11}^3) \\ &\quad +a_6(E_{22}^3)+a_7(E_{12}^3+E_{21}^3)+a_8(E_{11}^3E_{22})+a_9(E_{11}E_{22}^3)\big]\ . \end{aligned} \tag{2}$$

where E_{ij} $(i,j=1,2,3)$ are the components of the Lagrangian strain and C and a_i $(i=1,\ldots,9)$ are material model coefficients.

To validate the proposed fabric strain-energy model, and its ability to model the mechanical characteristics of knitted fabric under tensile loads, uniaxial tensile tests were performed. Four different knitted fabric structures were tested in the mutually orthogonal warp and weft directions. The axial stress-strain curves and localized axial and transverse strains were recorded for each direction.

A genetic algorithm combined with a uniaxial tensile finite element model was utilized to find the best fit material model parameters for each fabric. Figure 1 shows the close correlations between experimental and model data obtained. Only fabric sample 2 correlated poorly, with a linear stress-strain relation observed in the weft direction (Fig. 1 A). Failure in this regard was due to the inability of the fabric model to represent linear elastic relations.

[*Position of Figure 1*]

2.2 Finite Element Models

2.2.1 Graft model

The graft model was used to find the static and dynamic compliance values and pressure-diameter curves for different adventitial reinforcing fabric material model coefficients C and a_i $(i = 1, \ldots, 9)$, Eq. (2), with a particular porous graft.

Figure 2 illustrates the element, boundary and load conditions used for the graft model. The model simulates the behavior of the porous graft structure reinforced externally with the fabric reinforcing. Due to the symmetry of the problem, only one half of the longitudinal section of the graft and a quarter of the graft in the circumferential direction was modeled.

[*Position of Figure 2*]

Eight-node continuum elements without twist were used to model the porous polymer structure, while four-node linear membrane elements without twist were used for the fabric reinforcing. Two load cases were utilized to simulate static and dynamic compliance loads. In both cases, a pre-defined longitudinal (axial) strain of 10 % was initially applied before an internal pressure was applied on the inner surface of the porous structure. For the static load case the internal pressure applied to the inner graft surface was linearly ramped from 0 to 300 mmHg (39996 Pa) over 30 seconds. This mimicked the physical static compliance test carried out on a graft. For the dynamic load case, the internal pressure on the graft lumen wall was linearly ramped from 0 to 100 mmHg (13332 Pa) over a period of four seconds, after which a pulsatile pressure wave, described by a seven-term Fourier series

$$\alpha = A_o + \sum_{1}^{6}(B_n \sin n\varpi(t - t_o)) \quad \text{for } t \geqq t_o, \quad \alpha = A_o \text{ for } t \leq t_o \ , \tag{3}$$

was applied to mimic the pressure pulse applied in physical studies. Here ϖ is the frequency ($\varpi = 15.14\,\text{rad/s}$ and period $T = 0.83s$), t_o the time at which cyclic load starts ($t_o = 0$), A_o the initial amplitude ($A_o = 13332\,\text{Pa}$), and B_n are the Fourier constants ($B_1 = 2418.5$, $B_2 = 691.0$, $B_3 = 230.33$, $B_4 = 115.17$, $B_5 = B_6 = 114.7$).

Symmetric boundary conditions were applied to the graft model, with the end nodes fully fixed, and the central nodes fixed in the axial direction, allowing no angular twist, while being free to move radially.

The graft element mesh was refined longitudinally with successive mesh refinements towards the fixed end, but remained uniform in the radial and circumferential directions. The level of mesh refinement was verified through mesh sensitivity studies ensuring acceptable numerical accuracy.

2.2.2 Fabric models

The circumferential and longitudinal tensile models were used to provide mutually orthogonal stress-strain curves of the optimized fabric reinforcing solution obtained from the graft model and the genetic algorithm. The stress-strain curves obtained from the circumferential and longitudinal models were then used to produce reinforcing fabrics for the physical studies.

Circumferential tension The finite element model corresponding to experimental circumferential tensile test performed on fabrics at 37°C is illustrated in Fig. 3 (A). Due to the geometry of the problem and loading conditions, a quarter of the model was analyzed. Two steps were used in the circumferential tensile model: an initial contact step, which established contact between the analytically rigid pin and the fabric, and a second step which displaced the top pin at a rate of 200 mm/min,[17,18] until 50% circumferential strain was obtained. A 'soft' contact model was used which takes the form of an exponential function for the pressure-clearance relation. This allowed for the

gradual transfer of load from the pin to fabric. The pin was assumed to be smooth and frictionless. The orientations of the optimized material properties obtained from the graft model solutions were mapped onto the membrane elements, ensuring that the fabric principal directions were in-plane with the membrane surface.

Longitudinal tension Longitudinal fabric sample lengths of 48.0 mm were clamped flat at the ends and subjected to uniaxial tension. Figure 3 (B) shows the full and quarter symmetric finite element model used to obtain curves of force per unit length vs. displacement curves for the fabric reinforcing in the longitudinal direction. The longitudinal tensile model used a single step, which displaced the end of the fabric tube at a strain rate of 200 mm/min[17,18] to 100 % axial strain.

A mesh refinement study was performed on each of the finite element models. Critical nodes were monitored and mesh density was increased until the stress, strain and displacements observed became stable and consistent, thus reducing the error in model solutions.

[*Position of Figure 3*]

2.3 Optimization Using Genetic Algorithms

A genetic algorithm (GA) was used to optimize the fabric model coefficients C, a_i ($i = 1, \ldots, 9$) in Eq. (2) to obtain a dynamic compliance C_d of 6%/100 mmHg, a diastolic diameter d_{dia} of 4.0 mm, and to display nonlinear stiffening from a dynamic graft finite element model. The finite element analysis was executed with a particular fabric model with penalty and fitness functions of the GA. The process was repeated until a desired result was obtained or a pre-defined number of generations were reached. A number of 'good' solutions were then kept over the generations, and were then utilized in the tensile

test models to obtain a range of circumferential and longitudinal stress-strain curves for possible physical solutions for the fabric reinforcing.

The search space of the GA was dynamically adjusted over the generations; an initial range was set for each coefficient and thereafter the range was biased 3:2 between the first and second ranked solutions for the generation. The range of the search space was also reduced linearly, confining and refining the search area after each generation. The initial search space coefficient ranges were $0 < C \leqslant 20000$ and $0 \leqslant a_i \leqslant 20$, with the initial values $C = 10000$ and $a_i = 10$.

The model compliance (C_d) and nonlinear stiffening characteristic ($\jmath$) were calculated according to

$$C_d = \frac{d_{sys} - d_{dia}}{d_{dia}} \times \frac{100}{P_{sys} - P_{dia}} \times 100 \ , \tag{4}$$

$$\jmath = \frac{(d_{dia} - d_{init})(P_{sys} - P_{dia}) - P_{dia}(d_{sys} - d_{dia})}{P_{dia}} \ . \tag{5}$$

Here d_{init} is the initial internal diameter, d_{dia} and d_{sys} are the diastolic and systolic internal model diameters, and P_{dia} and P_{sys} are the diastolic and systolic pressures. Values of d_{dia}, d_{sys}, P_{dia} and P_{sys} were obtained from the dynamic graft finite element model analysis. The nonlinear stiffening characteristic $\jmath$ was the difference in diameter change per unit pressure from zero to P_{dia} and from P_{dia} to P_{sys}. C_d and d_{dia} were used to calculate the partial objective values for the model, while $\jmath$ was used as a penalty function.

From Eq. (4) a partial objective function formulated for compliance was given by

$$\phi^{\triangle C_d} = \left[1 - \left\{ |\triangle C_d^{norm}| \left(\frac{1}{(m^{\triangle C_d} - 1)} \right) \right\} \right] \ , \tag{6}$$

where

$$\triangle C_d^{norm} = \frac{C_d - C_d^{target}}{C_d^{target}} \tag{7}$$

and

$$m^{\triangle C_d} = \begin{cases} 1 + \left| \dfrac{C_d^{\max} - C_d^{target}}{C_d^{target}} \right| & \text{for } C_d > C_d^{target} \\ 1 + \left| \dfrac{C_d^{\min} - C_d^{target}}{C_d^{target}} \right| & \text{for } C_d \leq C_d^{target} \end{cases} . \tag{8}$$

From Eq. (6), $\phi^{\triangle C_d}$ tends to unity as C_d approaches C_d^{target}.

The partial objective function for the diastolic diameter was given by

$$\phi^{\triangle d_{dia}} = \left[1 - \left\{ \left| \triangle d_{dia}^{Normalized} \right| \left(\frac{1}{(m^{\triangle d_{dia}} - 1)} \right) \right\} \right] , \tag{9}$$

where

$$\triangle d_{dia}^{normalized} = \frac{d_{dia} - d_{dia}^{target}}{d_{dia}^{target}} , \tag{10}$$

$$m^{\triangle d_{dia}} = \begin{cases} 1 + \left| \dfrac{d_{dia}^{\max} - d_{dia}^{target}}{d_{dia}^{target}} \right| & \text{for: } d_{dia} > d_{dia}^{target} \\ 1 + \left| \dfrac{d_{dia}^{\min} - d_{dia}^{target}}{d_{dia}^{target}} \right| & \text{for: } d_{dia} \leq d_{dia}^{target} \end{cases} . \tag{11}$$

Like Eq. (6), Eq. (9) tends to unity as the model diastolic diameter d_{dia} tends to the target diastolic diameter d_{dia}^{target}.

The parameters $m^{\triangle C_d}$ and $m^{\triangle d_{dia}}$ were multiples used to bias future generations from a certain side and partially to penalize $\phi^{\triangle C_d}$ and $\phi^{\triangle d_{dia}}$, respectively. For example, due to tissue ingrowth in the porous grafts, compliance will be reduced after implantation; thus higher compliance values at time of implantation are preferred. These parameters were also used to partially penalize $\phi^{\triangle C_d}$ and $\phi^{\triangle d_{dia}}$ by making them negative if model C_d or d_{dia} go above or below pre-defined boundary values $C_d^{\max}$and $C_d^{\min}$. Thus,

$$\begin{aligned} &\text{if } \left\{ C_d \mid C_d \leq C_d^{\min} \text{ and } C_d \geq C_d^{\max} \right\} \text{ then } \phi^{\triangle C_d} \text{ was negatively weighted} , \\ &\text{if } \left\{ d_{dia} \mid d_{dia} \leq d_{dia}^{\min} \text{ and } d_{dia} \geq d_{dia}^{\max} \right\} \text{ then } \phi^{\triangle d_{dia}} \text{ was negatively weighted} . \end{aligned} \tag{12}$$

From these partial objective functions an objective function

$$\phi^{GA} = \frac{\left(w^{C_d} \times \phi^{\triangle C_d^{dyn}}\right) + \left(w^{d_{dia}} \times \phi^{\triangle d_{dia}}\right)}{\left(w^{C_d} + w^{d_{dia}}\right)} \tag{13}$$

was used to calculate the objective value, where w^{C_d} and $w^{d_{dia}}$ were pre-defined weightings used to bias the objective value to either the compliance or diastolic diameter. From Eq. (13), ϕ^{GA} will tend to unity as $\phi^{\triangle C_d^{dyn}}$ and $\phi^{\triangle d_{dia}}$ tend to unity.

The global penalties used were as follows:

$$\text{if} \begin{cases} C_d \leqslant 0.0\,\text{mmHg} \\ C_d = C_d^{target} \\ d_{dia} = d_{dia}^{target} \\ \jmath \leqslant 0.0 \end{cases} \quad \text{then } p^{GA} = -\infty, \text{ else } p^{GA} = 1 \tag{14}$$

Equation (14_1) ensured that the finite element results gave an expected positive compliance. With Eqs. (14_2) and (14_3), although we were optimizing for C_d^{target} and d_{dia}^{target}, due to numerical errors, such as round-off, these exact solutions will never be achieved. Equation (14_4) ensured that those solutions which did not display nonlinear stiffening were dismissed. Thus these penalties ensured that models which did not converge or do not show nonlinear stiffening were eliminated from future generations, while the partial penalties described by Eqs. (12) and (14) only weight a solution negatively, but do not necessarily expel the solution from future generations.

The fitness function used to compare the finite element solutions obtained was defined by

$$\text{Fitness Function } f^{GA} = p^{GA} \times \phi^{GA}. \tag{15}$$

Termination of the GA was set when a fitness value $f(C, a_i)$ of 0.95 or 50 generations were achieved. Typically, good solutions were found within 35 generations for the GA.

2.4 Manufacture and Characterization of Reinforcing Fabrics

2.4.1 Manufacture of fabric socks

Fabric socks were manufactured using braiding and knitting processes, respectively, (Secant Medical LLC, Perkasie, PA, USA) according to the required specification including longitudinal and circumferential force-displacement characteristics, inner diameter, fabric wall thickness, fiber thickness, pore size and surface coverage. The force-displacement characteristics of the manufactured prototypes were determined experimentally. In an iterative process, the comparison of the experimental data with the numerically predicted requirements was utilized to select the most promising prototype candidates and to guide the manufacturing of subsequent fabric generations.

2.4.2 Mechanical characterization of fabric socks

Longitudinal and circumferential tensile test were conducted using an Instron 5544 universal testing machine (Instron Corp., Norwood, MA, USA) in phosphate-buffered saline solution at 37 °C) to determine the force-displacement relationships in the two principal directions of the fabric socks. For circumferential tests, samples (length: 36.0 mm) were placed over two pins whereas for longitudinal tensile tests, samples (length: 48.0 mm) were clamped flat at both ends using custom-made fabric clamps. The cross-head speed was 200 mm/min[17,18] for all tests. The samples were tested to a maximum strain of 50% and 100% for circumferential and longitudinal tests, respectively.

2.5 Manufacture and Characterization of Graft Samples

2.5.1 Manufacture of graft samples

The non-reinforced graft samples comprised a 50 mm porous graft sections (manufactured as described in section *Porous polymer graft structures*) and two 20 mm e-PTFE graft anastomoses (inner diameter: 4 mm, wall thickness: 30 μm; Atrium, Hudson, NH).

The e-PTFE sections anastomosed to the porous graft by repeated application and drying of a polyurethane solution (5 % PUR by mass in Chloroform) while the segments were constrained on a central mandrel. The e-PTFE graft ends ensured a) that graft samples were not damaged due to attachment in the test fixture and b) consistent longitudinal strains during testing.

The reinforced samples utilized non-reinforced porous graft samples. Fabric socks were applied gently and gradually over the porous grafts ensuring uniformity. At one of the anastomotic regions of the porous graft, the fabric was anastomosed to the structure by additional application of a polyurethane solution (10 % PUR by mass in Chloroform). A higher concentrated polyurethane solution was used to reduce the absorption into the porous structure. Once this anastomotic region was cured, the fabric sock was strained, by uniformly and evenly stretching the fabric over the graft sample to the required amount, constrained by clamping, and fixed to the porous graft by applying repeated layers of polyurethane solution.

2.5.2 Measurement of graft compliance

In-vitro static and dynamic compliance tests were conducted using a custom-built test rig featuring a closed flow loop system (phosphate buffered saline, 37 °C).[29] For static tests, the range of the internal pressure was 0-200 $mmHg$. For dynamic tests, pressure of 80-120 $mmHg$ or equivalent pressure values accounting for the luminal latex liner(as described further below in this section). During the tests, the outer diameter of the graft samples was monitored with macroscopic digital imaging (Leica MS5 stereo microscope (Leica, Wetzlar, Germany), Sony CCD-IRIS digital camera (Sony, Tokyo, Japan), Strata Videoshop (Strata, Santa Clara, UT, USA)). In general, the compliance was determined using the inner diameter values. These were calculated from the measured outer graft diameter, the wall thickness and numerically predicted wall compression. In addition, the compliance was based on the outer graft diameter for a selected experiments for

comparison purposes.

Custom-made latex liners (outer diameter: $3.62 \pm 0.15\,mm$, wall thickness: $0.19 \pm 0.02\,mm$; Roynhardt Pvt. Ltd., Johannesburg, South Africa) were inserted into the graft samples to prevent pressure loss due to the porosity of the graft walls during the test procedure. The stiffening effect of the latex liner was compensated using the following procedure during a preliminary static compliance test for each graft sample:

1. Subtraction of pressure-diameter curves of the latex liner from the pressure–diameter curves of the graft sample with latex liner

2. Calculation of equivalent pressure values for the graft–liner samples corresponding to diastolic and systolic pressure of 80 and 120 mmHg for a graft sample without latex liner.

The equivalent diastolic-systolic pressure values used in dynamic compliance tests were 126-203, 144-218 and 163-243 $mmHg$ for the non-reinforced graft samples and 83-128, 102-150 and 116-168 $mmHg$ for the fabric-reinforced samples (for porogen size groups of 90-106, 106-125 and 125-150 μm, respectively).

2.6 Validation of Numerical Solutions

In order to account for differences of the mechanical characteristics between the optimal fabric solutions proposed numerically and the manufactured fabric sock prototypes, the coefficients of the fabric material model were adjusted, using a genetic algorithm, so as to optimally represent the mechanical characteristics of the prototypes determined experimentally.

This GA utilized similar partial objective and fitness functions as the algorithm described above, but differed in the procedure as the fitness and objective functions were optimized for axial and transverse stress-strain data collected for the prototype fabric socks.

Subsequently, revised numerical solutions for fabric-reinforced grafts were obtained using the prototype fabric material coefficients. The numerical predictions for the graft compliance were compared with the results of the in-vitro compliance tests providing a measure for agreement between model and experiment.[19]

3 Results

3.1 Non-reinforced Porous Graft Finite Element Models

Table 1 gives the dynamic and static compliance values obtained from the graft numerical models for each of the porous graft structures without fabric reinforcing. Other values displayed include wall compression and diastolic and systolic internal diameters.

[*Position of Table 1*]

The compliance increases with increased pore size. Little difference was observed between the dynamic and static compliance values; however, as pore size increased, a slight increase was seen in static compliance. Diastolic and systolic internal diameters reflected similar characteristics with respective static and dynamic compliance. However, there was a large difference between the static and dynamic wall compression values obtained; for dynamic values the compression observed was much lower, due to the lagging wall response with pressure pulse observed in the dynamic numerical models.

Figure 4 (A-C) displays the dynamic circumferential, radial and axial stress fields through the various pore size non-reinforced graft structures at mean internal pressure (100 mmHg). The stress fields and sizes are displayed to the same scale to highlight the difference in field and diameters. The profiles of circumferential, radial and axial stress are illustrated in Fig. 4 (D-F) for the various porogen size non-reinforced graft structures.

[*Position of Figure 4*]

The contour plots and graphs in Fig. 4 indicate that the circumferential stress increased with increased pore size, with the difference between the 90-106 and 106-125 μm being less than that observed between the 106-125 and 125-150 μm. The magnitude of the radial stress for each pore size group was equal through the wall thickness. It was also observed that the axial stress fields decreased considerably in magnitude with increased pore size. The shape of the circumferential and radial stress profiles through the graft wall were similar for increasing pore size. However, a variation in axial stress profiles was observed between the pore size grafts. The stronger 90-106 μm porogen size graft had a higher axial stress at the luminal surface which decayed towards the adventitial surface, while the axial stress profiles through the wall were almost constant for the weaker 106-125 and 125-150 μm. Thus, the weaker large porogen grafts appeared to distribute the axial load more evenly through the wall.

Figure 5 (A) shows curves of static pressure vs. normalized change in internal diameter (P vs. $\triangle d/d_o$) for the individual porogen size grafts. The non-reinforced porous grafts displayed no stiffening characteristics, thus becoming weaker at higher pressures.

[*Position of Figure 5*]

3.2 Optimized Model Solutions for Fabric Reinforced Grafts

After implementing the GA, a total of 38, 31 and 29 generations were required before reasonable solutions were obtained for increasing porogen size grafts, respectively. A further 8 and 5 generations were required, respectively, to attain the desired 0.95 fitness value for the 106-125 and 125-150 μm graft types; however, the full 50 generations were needed before the 90-106 μm graft type obtained a 0.948 fitness value. Table 2 displays the optimal fabric model solutions obtained from the GA for each of the pore size grafts.

The table includes compliance values, internal graft diameter, wall compression, fabric circumferential strain, model coefficients, and fitness and objective values obtained.

[*Position of Table 2*]

The results obtained from the GA gave dynamic diameter compliance values of 6.4, 6.9 and 7.1 %/100 mmHg and diastolic diameters of 3.965, 3.998 and 4.000 mm for the fabric reinforced 90-106, 106-125 and 125-150 μm porogen grafts, respectively. A maximum wall compression of 6.20 % was observed for the 125-150 μm porogen graft. The circumferential strain in the fabric reinforcement was greatest for the reinforced 106-125 μm porogen graft, with a value of 8.85 %, while values of 8.13 % and 8.70 % were observed for the reinforced 90-106 and 125-150 μm porogen grafts, respectively. In contrast, the internal diameter at the systolic pressure was less for the 90-106 and 106-125 μm grafts than for the 125-150 μm porogen graft, implying that the adventitial reinforcing fabric plays a larger role in the weaker structures, or increased pore size.

Figure 6 displays the dynamic circumferential, radial and axial stress through the wall thickness for the various pore size adventitial fabric reinforced grafts at mean pressure (100 mmHg). The high fabric stress values, indicated by the sharp change in stress profile in Fig. 6 (D) and (F), obtained for the 125-150 μm reinforced graft compared to the 106-125 and 90-106 μm structures, illustrated that the fabric reinforcing played a dominant role in the weaker 125-150 μm graft, while this role was reduced in the 106-125 and 90-106 μm structures.

[*Position of Figure 6*]

Comparing Fig. 4 (D-F) and Fig. 6 (D-F), the fabric reinforcing reduced and leveled out the circumferential stresses for all porogen sizes. The axial stress was similarly

reduced for all porogen sizes whereas leveling out of axial stress was only observed in the 125-150 μm graft but not in the 106-125 and 90-106 μm structures. With the addition of the reinforcing, the compressive radial stress increased toward the outer (adventitial) surface, while relatively small changes were observed at the lumen for all graft types.

The fabric model solutions obtained from GA were utilized in static numerical graft models to obtain curves of static pressure vs. normalized change in diameter for the reinforced 90-106, 106-125 and 125-150 μm porogen grafts. Figure 5 (B) displays the internal and external diameter curves obtained for the various structures. The onset of nonlinear stiffening is indicated in the graph. The grafts exhibited nonlinear stiffening characteristics when the fabric reinforcing was utilized as compared to a linear pressure-diameter change relationship for the non-reinforced graft. The onset of nonlinear stiffening of the reinforced grafts was predicted at ca. 35 mmHg luminal pressure, i.e. far below the physiological range, for all three pore size groups. The difference in nonlinear stiffening between the internal and external diameter curves was apparent, where the internal stiffening was not as pronounced due to compression of the graft wall.

3.3 Circumferential and Longitudinal Model Solutions

The three highest ranked fabric model solutions obtained from the GA were implemented in the circumferential and longitudinal tensile numerical models to obtain the fabric requirements in terms of force per unit length vs. displacement for porous grafts of each porogen size group. These force per unit length vs. displacement curves were used to develop physical fabric reinforcing samples.

3.3.1 Circumferential stress-strain curves

Figure 7 displays normalized force (i.e. per unit length) vs. strain in the circumferential and longitudinal direction, respectively, for the three best fabric reinforcing solutions obtained from the GA for the 125-150 μm porous structure. The circumferential force-

strain curves were very similar, Fig. 7 (A), however, a large difference was observed in the longitudinal force-strain curves for the three solutions, Fig. 7 (B). Table 3 exhibits the variation in compliance, wall compression, internal diameter, fabric circumferential strain and the fitness values of the first three fabric reinforcing solutions for the 125-150 μm graft.

[*Position of Figure 7*]

[*Position of Table 3*]

A number of reinforcing solutions were possible to obtain the desired compliance, diastolic diameter and nonlinear stiffening characteristics for a particular porous structure. Figure 5 (C) illustrates the different pressure-diameter relations obtained from the first three reinforcing solutions for the 125-150 μm graft. Slight variations were observed in the curvature, however the compliance and diastolic diameter requirements were consistent for each solution as indicated in Table 3.

Figure 8 shows the circumferential and longitudinal tensile test response of the fabric reinforcing solutions obtained from GA for the different pore size graft types (see Table 2). Pronounced differences were observed between the required fabric reinforcing for each pore size graft for both loading cases. A large change was observed in force per unit length at 16, 18 and 20 % circumferential strain for increasing pore size, respectively, in the circumferential direction (Fig. 8 (A)). The circumferential transverse strains were high for the 90-106 and low for the 106-125 μm graft types reinforcing solutions. In the longitudinal direction, the required fabric reinforcing stiffened much earlier for the 125-150 μm graft compared to the 90-106 and 106-125 μm reinforcing solutions, and the longitudinal transverse strains were high for the 125-150 μm fabric reinforcing, see Fig. 8 (B).

[*Position of Figure 8*]

3.3.2 Stress fields for reinforcing fabrics

Figure 9 (A) depicts the circumferential ($S22$), axial ($S11$) and shear ($S12$) stress fields for the fabric circumferential tensile model solution for the 125-150 μm graft obtained from the GA (see Table 2). The stress fields were reasonable, where the maximum stress values observed were in the circumferential direction. This circumferential stress was maximum at the center and reduced toward the edge of the fabric reinforcing tube. The distribution of longitudinal stress was similar, where a maximum was observed at the center. Both the circumferential and longitudinal stress fields were in tension and the circumferential stress was roughly 25 times higher than the longitudinal stress.

Figure 9 (B) displays the axial ($S11$) and circumferential ($S22$) stress fields and the deformed and undeformed configurations of the fabric longitudinal tensile model solution for the 125-150 μm graft. Again, realistic deformation in the circumferential direction was observed due to longitudinal tension. The axial stress field observed was maximum at the center of the fabric reinforcing tube (if one ignores edge effects due to model constraints), while circumferential stress was observed to be a maximum at the clamped end. The maximum longitudinal stress was 3×10^6 times higher than the maximum circumferential stress.

[*Position of Figure 9*]

3.4 Prototypes of Fabric Reinforcing Socks

From an initial generation of 16 different fabric socks, six designs were identified as potential candidates to comply with the required specification with respect to force-displacement characteristics and promotion of tissue ingrowth. A refined evaluation

resulted in exclusion of four of the six fabric sock designs from further optimization. The shortlisted two designs underwent two iterations of design adjustment, manufacturing and experimental assessment.

The final generation of the two prototype designs (prototypes I and II) featured knits of Dacron fiber threads (fiber diameter: $50\,\mu$m) with pore diameter of 0.35 mm and surface coverage of 70 - 75%. To enable a feasible assembly procedure of the fabric sock and the porous graft structure (OD: 5.0 mm), it was found that an inner diameter of the fabric socks of 6.0 mm was preferential to the value of 5.0 mm predicted numerically. The difference in inner diameter of the sock and outer diameter of the graft was accommodated by longitudinally stretching the fabric sock by $59 \pm 1.9\,\%$ (prototype I) and $91 \pm 1.7\,\%$ (prototype II) during the assembly procedure.

Figure 10 (A) displays the circumferential force-displacement curves of the two prototype socks, without (i.e. as manufactured) and with longitudinal pre-strain, and the optimal fabric model solution for the graft of 90 -106 μm porogen size.

[*Position of Figure 10*]

3.5 Validation of Numerical Results

Figure 10 (B) and (C) display experimental data and the he fabric model solutions with optimized coefficients obtained from the GA for the fabric prototypes I and II with pre-straining. The models represented the physical behavior of the fabrics very well in circumferential direction (Fig. 10 B). For longitudinal tension (Fig. 10 C), the agreement between model and experiment was reasonable for longitudinal strains up to approximately 60%.

Using these fabric model solutions, the FE model for fabric-reinforced grafts predicted compliance values that deviated from those obtained with the optimal fabric model solutions (see Table 2).

Table 4 presents the static and dynamic compliance values numerically, predicted and experimentally measured, for non-reinforced grafts and grafts reinforced with prototype I fabric socks. For the compliance based on inner graft diameter, $C_{d,dyn}$(ID) and $C_{d,stat}$(ID), the numerical models markedly overestimated the compliance in all cases. The overestimation was more pronounced in the fabric-reinforced grafts compared to the non-reinforced grafts, except for the largest porogen size class 125-150 μm. The the variation between numerical and experimental values increased with increasing porogen size for the non-reinforced grafts whereas the variation decreased with increasing porogen size for the fabric-reinforced grafts.

A considerable better agreement between numerical and experimental results was obtained when the compliance, $C_{d,stat}$(OD), was calculated using the outer diameter of the graft. This was demonstrated for the static case. The improvement was more apparent for the non-reinforced grafts compared to the reinforced grafts.

[*Position of Table 4*]

4 Discussion

4.1 Genetic Algorithm for Fabric Reinforced Graft Compliance

The search features of the GA were: dynamic search space, a step-wise increase in search space resolution after n generations and a linear reduction in search space range after each generation. The dynamic search space allowed the genetic algorithm to adjust the search boundaries after each generation. The boundaries were redefined between the first and second ranked solutions with a 3:2 bias towards the first ranked solution after each generation. Implicit constraints were imposed on these boundaries, ensuring that certain coefficients remain positive, such as coefficient C. This dynamic search space was seen as

a major advantage as model coefficients diverged considerably from the initial starting values as observed in Table 2. The step-wise increase in search space resolution was implemented to search a coarse grid over n generations before being refined. With the linear reduction of search space range after each generation it was found that step-wise increasing resolution after n generations was not necessarily effective, as this limited the widespread searching capabilities of the GA. The implementation and magnitude of the GA features can easily be adjusted. Although no extensive study was performed on the adjustment of these parameters, a qualitative study revealed that utilizing the dynamic search space was beneficial where an initial low resolution and linear reduction in range gave better results. The step-wise increase of resolution and a fixed small search range should only be implemented when a reasonable solution was found, thus increasing the resolution used to refine the obtained solution.

The magnitudes of the parameters used to control the GA can easily be adjusted. Thus, weightings for the partial objective functions can be adjusted accordingly, allowing the GA to optimize on certain criteria first or in a biased fashion. For example, the partial objective functions for C_d and d_{dia} were weighted toward C_d allowing the GA to optimize on C_d first and then refine for d_{dia} later. It was found that adjusting the partial objective weightings changed the solutions obtained.

The GA was automated to save a number of ranked solutions in each generation and grade them into a global solutions array. Once a predefined fitness value was achieved (typically 0.95) or a number of generations reached, the GA analyzed the global solutions in a number of numerical models. The GA not only utilized a dynamic graft model, it also generated circumferential and longitudinal tensile simulations and a number of static and dynamic graft models using the global solutions. Not all the global solutions solved in the circumferential and longitudinal tensile simulations or the static and dynamic graft models. Thus, a number of the global solutions were annulled, due to their in-ability to converge in other finite element models, reducing the number of possible solutions.

The GA optimizing for an objective function in terms of dynamic diameter compliance C_d, diastolic diameter, and nonlinear stiffening characteristic in a dynamic graft model, was directly dependent on the behavior of the graft internal diameter with pressure and indirectly dependent on the wall compression and longitudinal changes. This has areas of weakness in terms of the graft's in-vivo application and the test results obtained from in-vitro tests. For example, the effects of fixing both ends must be assessed against physiological situations in which anastomoses will never be fixed. If appropriate physiological data is available, requirements for the longitudinal changes observed in native blood vessels and the limit for wall compression of the porous structure to promote tissue ingrowth can be implemented into the objective function. These requirements may then be weighted accordingly to find those solutions which give a required compliance, optimal wall compression and axial strain. Another possibility is that of optimizing on the nonlinear stiffening index β defined by Hayashi *et al.*,[11] rather than compliance. As a benefit, the nonlinear stiffening requirements would be incorporated in the objective function rather than as a penalty, as was implemented in the GA.

Although the optimal solutions were intended to describe a fabric reinforcing, the solutions obtained from the GA can also be used to find materials and structures which behave in a similar fashion. Thus, the adventitial reinforcing solutions need not be restricted to fabrics, but can be used for other structures as long as their application does not limit other features, such as cellular ingrowth through the reinforcing structure and into the porous graft.

4.2 Fabric Constitutive Model

The fabric model gave an indication for the requirements of an ideal fabric reinforcing for a compliant, adventitial-styled graft.

It was found from a patch test study and the sample solutions of the fabric material model that a number of the coefficients, viz. C, a_1, a_2, a_3 and a_4 should remain posi-

tive to ensure realistic fabric uniaxial tensile solutions. Negative coefficients produced unrealistic compressive stresses and negative Poisson's effects under tension.

However, the fabric model failed to model fabrics with linear stress-strain relations. To possibly overcome this, a combined polynomial and exponential function could be used as described by Tong and Fung.[7] This strain energy function was shown to give greater anisotropic behavior and variation in relations in the transverse directions. Thus, a similar function could be utilized to cater for the linear stress-strain components. However, 13 coefficients would need to be solved for when using this function, instead of 10 terms in function used here. One of the terms may also cause unrealistic fabric behavior due to 'polynomial wiggling'.[6]

When implanted in the body, the physical behavior of the fabric will change considerably over time, as cells seed themselves to the fabric, changing its mechanical nature. Thus, a time-dependent model for tissue ingrowth should be incorporated in the constitutive relation, where with time, an increase in stiffness can be included by increasing C, while, the orthogonal anisotropic nature and orientation may be adjusted by varying the a_i coefficients suitably. The nature of this change with time will require extensive experimental data to obtain realistic relations, with variation in material type and fabric construction.

4.3 Numerical Solutions for Non-reinforced and Fabric-reinforced Grafts

Supra-physiological diametric compliance was observed for the non-reinforced grafts with 16.0, 19.2, and 31.5 %/100mmHg for the 90-106, 106-125, and 125-150 μm porogen size porous structures, indicating a structural weakening with increasing pore size. The adventitial fabric reinforcement reduced the diametric graft compliance by 60, 64, and 77 % to 6.4, 6.9, and 7.1 %/100mmHg (90-106, 106-125, 125-150 μm porogen size) which agrees very well with the target compliance of 6.0 %/100mmHg. The high compliance of the non-reinforced grafts was linked to excessive dilation with a potential for lumi-

nal mismatch between graft and host vessel. The target internal diameter at diastolic pressure (4.0 mm) was exceeded by 1.6, 3.3, and 8.6 % (4.06, 4.13, 4.34 mm). At systolic pressure, the grafts dilate to 4.32, 4.45, and 4.88 mm, i.e. 5.1, 8.5, and 19.2 % beyond the target value of 4.1 mm which was derived from target diastolic diameter and target compliance.

For the fabric reinforced grafts, diastolic (3.97, 4.0, 4.0 mm) and systolic internal diameter (4.07, 4.11, 4.11 mm) agreed very well with the target diameter values. The diameter of the 90-106 μm porogen reinforced graft remains 0.9 % (diastole) and 0.7 % (systole) below the target while the target diameter was exceeded maximally by 0.42 % for the 125-150 μm porogen graft at systolic pressure.

The non-reinforced grafts do not display stiffening characteristics, see Fig. 5 (A). The deviation between predicted and target diameter was more pronounced at systolic pressure than at diastolic pressure. This illustrated a weakening of the grafts with increasing pressure and an inability to withstand increased circumferential forces acting on the graft wall at larger diameters. In contrast, non-linear stiffening was numerically predicted for the reinforced grafts, with the onset of the stiffening below diastolic pressure, featuring an arterial-like pressure-diameter relationship.

4.4 Validation

The comparison with experimental results indicated that the numerical solutions predicted higher values for the graft compliance for most of the cases studied. For the non-reinforced grafts it was observed that a considerably improved agreement between model and experiment was achieved when the outer graft diameter, instead of the inner diameter, was used for compliance calculations. The relative differences decreased from 64.7 ± 38.9 % to 4.5 ± 10.6 % (average for the three porogen size groups). For the fabric-reinforced grafts, the relative differences observed were larger and the change of diameter reference resulted in a less pronounced improvement from 168.8 ± 139.6 % to

$116.0 \pm 164.4\,\%$. The best agreement for reinforced grafts was however achieved for the dynamic compliance with $95.2 \pm 52.2\,\%$

In view of the markedly different compliance values for the non-reinforced and the fabric-reinforced grafts, the absolute differences between experiments and models were reviewed additionally. For the dynamic compliance based on inner diameter, the model predictions exceeded the experimental results on average merely by $2.6 \pm 0.6\,\%/100\,\mathrm{mmHg}$ for the grafts with fabric reinforcement and by $8.4 \pm 6.9\,\%/100\,\mathrm{mmHg}$ for the non-reinforced grafts. These values indicated in fact an acceptable agreement, in particular for the fabric-reinforced grafts. For the static compliance associated with the change of inner diameter, the absolute difference decreased to similar values of $0.7 \pm 1.0\,\%/100\,\mathrm{mmHg}$ and $0.6 \pm 1.3\,\%/100\,\mathrm{mmHg}$ for the reinforced and the non-reinforced grafts, respectively.

Despite the satisfactory agreements of the absolute differences, various parameters were identified as potential factors for the deviations. The fabric models did not optimally represent the physical behavior of the fabric prototypes I and II in longitudinal tension for strains exceeding 60%, see Fig. 10 (C). In addition, the fabric model solutions were not optimized for transverse strain due to lack of experimental data for the sock samples. The mechanical characterization of the porous polymer was performed on samples prepared from cast rods as compared to the grafts which were cast as tubes. This may have caused different material/structural properties due to potentially varying packing configurations of the porogen. The latex liners obtained and used for compliance testing of the graft samples displayed a variation in mechanical properties. Furthermore, applying longitudinal strain to the graft samples according to the protocols for compliance testing may have caused the luminal latex liners to collapse inside the graft sample affecting the graft's behavior. An appreciable variation of the experimental results, indicated by the large standard deviations of the measured compliance values (Table 4), may also be attributed to the intensive manual processes during manufacturing of the graft samples.

4.5 Relevance for Tissue Engineering

The wall compression at systolic pressure (during dynamic loading) was predicted to be 5.68, 6.51, and 8.77 % in non-reinforced porous grafts (Table 1) and 4.82, 5.31, and 6.20 % in the fabric reinforced grafts (Table 2) for the 90-106, 106-125, and 125-150 μm porogen size group. These values represented a reduction of wall compression in the reinforced grafts by 15.2, 18.4, and 29.3 % compared to the non-reinforced grafts of the three porogen size groups. Considering that the predicted dilation was larger in the non-reinforced grafts compared to the reinforced grafts, these findings indicated that the wall compression was predominantly governed by the dilation of the graft inducing transverse wall contraction. The compression of the wall due to internal pressure load played a secondary role even in samples with fabric reinforcement. The reduced wall compression in reinforced samples also suggested that the fabric reinforcement contributed to maintaining the dimensions of the interconnected pores required for tissue ingrowth.

The diameter of interconnecting pore windows was on average 0.52 ± 0.04 % of the porogen diameter.[1] For the porous grafts of the 90-106, 106-125, and 125-150 μm porogen size, the minimum pore window diameter was approximately 47, 55, and 65 μm. With the predicted wall compression at systolic pressure, the minimum pore window sizes, available for cellular ingrowth, decrease to 44, 52, and 59 μm in the non-reinforced porous grafts feature (while the minimum window size was slightly larger in the reinforced porous structures due to the lower wall compression). The average diameter of a capillary is 8-10 μm, while the diameter of a functional arteriole, endothelium and a single layer of smooth muscles is roughly 30 μm.[7,8] Thus, all three pore size graft groups permit ingrowth of arterioles, endothelial cells and smooth muscle cells.

The ingrowth of tissue, a process desired with the presented porous structures, was not included in this study. Vascularization and cellular ingrowth will affect the mechanical graft properties in-vivo. As such, these processes are important to be considered for

the optimization of these porous grafts. The development and incorporation of a time dependent constitutive model to account for tissue ingrowth offers itself as future scope for this research.

5 Conclusions

The objective of this study was to find an optimal structural design of a tissue-regenerative vascular prosthesis exhibiting arterial-like mechanics. Adopting from native arteries a layered structure of intima/media and adventitia, the challenge was to identify the mechanical characteristics of an adventitial fabric layer that provide together with the given properties of a porous polymeric intima/media layer the desired biomechanical properties of the graft structure.

It was shown that by combining finite element methods and genetic algorithms, complemented with experimental methods, the required mechanical characteristics of the adventitial fabric reinforcement can be specified. The finite element methods were used to study the structural mechanics of the two-layer graft system whereas the genetic algorithms served to optimize the mechanical characteristics of the adventitial fabric. As part of this numerical framework, experimental methods were employed to determine constitutive material parameters.

Beyond the demonstration of the feasibility of numerical method, it was shown that the graft system of adventitially reinforced polymer with well-defined interconnected porosity can be expected to facilitate the ingrowth and regeneration of tissue such as arterioles, endothelial cells and smooth muscle cells for all pore sizes studied.

While the presented problem focused on the optimization of a fabric-type layer, the numerical solutions may be applied to other materials and structures, functioning as an adventitial reinforcement. Furthermore, the numerical method offers potential for the application to optimization problems with different concepts of modular, or compos-

ite, vascular prostheses. This may, in particular with emphasis on tissue regeneration, include the consideration of the biodegradation of the prosthetic materials and the incorporation of tissue in the initial mechanical design of vascular prostheses.

Acknowledgments

This work was mainly funded through a research collaboration grant by Medtronic Inc. (Minneapolis, MN, USA) to the University of Cape Town. The authors acknowledge the assistance of Richard Steventon with the GA coding.

References

[1] D. Bezuidenhout. *Porous Polymeric Superstructures as In-Growth Scaffolds for Tissue-Engineered Vascular Prosthesis*. PhD thesis, Stellenbosch University, 2001.

[2] D. Bezuidenhout, N. Davies, and P. Zilla. Effect of well defined dodecahedral porosity on inflammation and angiogenesis. *ASAIO J*, 48:465–71, 2002.

[3] W.E. Burkel. The challenge of small diameter vascular grafts. *Medical progress through technology*, 14:165–175, 1988.

[4] N. Davies, S. Dobner, D. Bezuidenhout, C. Schmidt, M. Beck, A.H. Zisch, and P. Zilla. The dosage dependence of vegf stimulation on scaffold neovascularisation. *Biomaterials*, 29:3531–3538, 2008.

[5] M. Deutsch, J. Meinhart, P. Zilla, N Howanietz, M. Gorlitzer, A. Froeschl, A. Stuempflen, D. Bezuidenhout, and M. Grabenwoeger. Long-term experience in autologous in vitro endothelialization of infrainguinal eptfe grafts. *J Vasc Surg*, 49:352–62, 2009.

[6] J.D. Faires and R.L. Burden. *Numerical Methods*. PWS Publishing, Boston, 1993.

[7] Y.C. Fung. *Biomechanics: Mechanical Properties of Living Tissue*. Springer-Verlag, New York, 2nd edition, 1984.

[8] J. Gamble, L. Matthias, G. Meyer, P. Kaur, G. Russ, R. Faull, M. Berndt, and M. Vadas. Regulation of in vitro capillary tube formation by anti-intergrin antibodies. *J. Cell Biol.*, 121:931–943, 1993.

[9] J.E. Hasson, J. Megerman, and W. A. Abbott. Increased compliance near vascular anastamosis. *J. Vasc. Surg.*, 2:419–423, 1985.

[10] K. Hayashi. Experimental approaches on measuring the mechanical properties and constitutive laws of arterial walls. *J. Biomech. Eng.*, 115:481–487, 1993.

[11] K. Hayashi, H. Handa, S. Nagasawa, A. Okumura, and K. Moritake. Stiffness and elastic behavior of human intracranial and extracranial arteries. *J. Biomechanics*, 13:175–184, 1980.

[12] F. Hess, C. Jerusalem, and B. Braun. The endothelialisation of a fibrous polyurethane microvascular prosthesis after implantation in the abdominal aorta of the rat. *J. Cardiovasc. Surgery*, 24:516–524, 1983.

[13] T.V. How, R. Guidon, and S.K. Young. Engineering design of vascular prosthesis. *Proc. Instn. Mech. Eng. [H]*, 206:61–71, 1992.

[14] C.-C. Hsu, C.-K. Chao, J.-L. Wang, and J. Lin. Multiobjective optimization of tibial locking screw design using a genetic algorithm: Evaluation of mechanical performance. *Journal of Orthopaedic Research*, 24:908–916, 2006.

[15] A.S. Khalil, B.E. Bouma, and M.R. Kaazempur Mofrad. A combined fem/genetic algorithm for vascular soft tissue elasticity estimation. *Cardiovascular Engineering*, 6:93–103, 2006.

[16] J.H. Kim. *Fabric Mechanics Analysis Using Large Deformation Orthotropic Shell Theory*. PhD thesis, North Carolina State University, 1991.

[17] NN. *Cardiovascular Implants - Vascular Prosthesis*. American National Standard Association for the Advancement of Medical Instrumentation, aami standard edition, 1994.

[18] NN. *Cardiovascular Implants-Tubular Vascular Prosthesis*. ISO International Standard 7198, 1998.

[19] W.L. Oberkampf and M.F. Barone. Measures of agreement between computation and experiment: Validation metrics. *Journal of Computational Physics*, 217:5–36, 2006.

[20] A. Pandit, X. Lu, C. Wang, and G.S. Kassab. Biaxial elastic material properties of porcine coronary media and adventitia. *American Journal of Physiology - Heart and Circulatory Physiology*, 288:H2581–7, 2005.

[21] K.B. Seifert, D. Albo, H. Knowlton, and D.J. Lyman. Effect of elasticty of prosthetic wall on patency of small-diameter arterial prosthesis. *Surg. Forum.*, 30:206–208, 1979.

[22] N. Siauve, L. Nicolas, C. Vollaire, and C. Marchal. Optimization of the sources in local hyperthermia using a combined finite element-genetic algorithm method. *International Journal of Hyperthermia*, 20:815–833, 2004.

[23] S.F.C. Stewart and D.J. Lyman. Effects of vascular Graft/Natural artery compliance mismatch on pulsatile flow. *J. Biomech.*, 25:297–310, 1992.

[24] B. Storåkers. On material representation and constitutive branching in finite compressible elasticity. *Journal of the Mechanics and Physics of Solids*, 34:125–145, 1986.

[25] N.R. Tai, H.J. Salacinski, A. Edwards, G. Hamilton, and A.M. Seifalian. Compliance properties of conduits used in vascular reconstruction. *Br J Surg*, 87:1516–24, 2000.

[26] A. Takahara, A.J. Coury, R.W. Hergenrother, and S.L. Cooper. Effect of soft segment chemistry on the biostability of segmented polyurethanes. i. in vitro oxidation. *J Biomed Mater Res*, 25:341–356, 1991.

[27] C. Wang, M. Garcia, X. Lu, Y. Lanir, and G.S. Kassab. Three-dimensional mechanical properties of porcine coronary arteries: a validated two-layer model. *American Journal of Physiology - Heart and Circulatory Physiology*, 291:H1200–H1209, 2006.

[28] M.W. Weston, K. Rhee, and J.M. Tarbell. Compliance and diameter mismatch affect the wall shear rate distribution near end-to-end anastomosis. *J. Biomech.*, 29:187–198, 1996.

[29] M.S. Yeoman. *The Design and Optimisation of Fabric Reinforced Porous Prosthetic Grafts Using Finite Element Methods and Genetic Algorithms.* PhD thesis, University of Cape Town, June 2004.

[30] P. Zilla, D. Bezuidenhout, and P. Human. Prosthetic vascular grafts: Wrong models, wrong questions and no healing. *Biomaterials*, 28:5009–27, 2007.

Table 1: Numerical predictions for diametric compliance, internal diameter, and wall compression of non-reinforced graft models for static and dynamic loading.

Graft Porogen Size (μm)	*90-106*		*106-125*		*125-150*	
	Stat	*Dyn*	*Stat*	*Dyn*	*Stat*	*Dyn*
$\mathbf{C}_d$ (%/100mmHg)	16.9	16.0	20.3	19.2	33.9	31.5
Internal Diameter ϕ_i (mm):						
Diastolic	4.088	4.064	4.160	4.133	4.378	4.342
Systolic	4.377	4.319	4.516	4.445	5.002	4.879
Wall Compression (%):						
Diastolic	5.46	1.91	6.25	1.97	8.31	1.28
Systolic	7.72	5.68	8.99	6.51	13.06	8.77

Table 2: Optimal solutions for fabric reinforced porous grafts of 90-106, 106-125 and 125-150 μm porogen obtained from GA.

Graft Porogen Size (μm)		*90-106*	*106-125*	*125-150*
Dynamic C_d ($\%/100mmHg$)		6.4	6.9	7.1
Internal Diameter ϕ_i (mm):	*Diastolic*	3.965	3.998	4.000
	Systolic	4.067	4.109	4.113
Wall Compression (%):	*Diastolic*	2.93	3.24	3.82
	Systolic	4.82	5.31	6.20
Fabric Circumferential Strain (%):				
	Diastolic	6.61	7.19	7.08
	Systolic	8.13	8.85	8.70
Fabric Model Coefficients:	C	607.969	977.145	3881.518
	a_1	0.028	15.885	17.748
	a_2	270.643	204.607	133.838
	a_3	1.719	21.012	6.662
	a_4	24.310	16.631	25.734
	a_5	2.745	-28.013	13.785
	a_6	64.376	50.642	66.498
	a_7	8.014	-24.693	-18.083
	a_8	-8.797	-13.284	2.018
	a_9	-9.155	14.190	20.619
Fitness Value:	$f(C, a_i)$	0.9484	0.9552	0.9509
Objective Value:	$\phi(C, a_i)$	0.9484	0.9552	0.9509
Partial Objective Values:	$\phi^{\triangle C_d^{dyn}}$	0.9693	0.9329	0.9230
	$\phi^{\triangle d_{dia}}$	0.9119	0.9943	0.9996
Generation Number		50	39	34
Total Time (hh:mm)		41 : 48	30 : 13	22 : 37

Table 3: Three best solutions obtained from the generations of the GA for fabric reinforced 125-150 μm porogen grafts

Solution Number		*1*	*2*	*3*
Dynamic C_d (%/100mmHg)		7.1	7.0	7.2
Internal Diameter ϕ_i (mm):	*Diastolic*	4.000	3.992	4.000
	Systolic	4.113	4.104	4.115
Wall Compression (%):	*Diastolic*	3.82	3.82	3.82
	Systolic	6.20	6.20	6.20
Fabric Circumferential Strain (%):				
	Diastolic	7.08	7.03	7.07
	Systolic	8.70	8.68	8.74
Fabric Model Coefficients:	C	3881.518	4282.589	4282.589
	a_1	17.748	13.737	12.918
	a_2	133.838	133.236	126.283
	a_3	6.662	2.250	2.554
	a_4	25.734	15.106	12.542
	a_5	13.785	18.598	14.050
	a_6	66.498	68.905	66.776
	a_7	−18.083	−11.465	−21.364
	a_8	2.018	11.242	4.791
	a_9	20.619	18.212	14.993
Fitness Value:	$f(C, a_i)$	0.9509	0.9451	0.9448
Objective Value:	$\phi(C, a_i)$	0.9509	0.9451	0.9448
Partial Objective Values:	$\phi^{\triangle C_d^{dyn}}$	0.9230	0.9257	0.9134
	$\phi^{\triangle d_{dia}}$	0.9996	0.9791	0.9997
Generation Number		34	32	30

Table 4: Static ($C_{d,stat}$) and dynamic ($C_{d,dyn}$) compliance of non-reinforced and prototype I fabric-reinforced graft samples from in-vitro compliance tests (Experiment) and numerical predictions (Model). The compliance values were based on inner graft diameter (ID) for the dynamic case and both inner (ID) and outer (OD) graft diameter for the static case.

	Non-reinforced grafts *Porogen size (μm)*			**Fabric-reinforced grafts** *Porogen size (μm)*		
	90-106	*106-125*	*125-150*	*90-106*	*106-125*	*125-150*
$\mathbf{C_{d,dyn}}$(ID)						
Experiment (%/100mmHg)	13.3±1.2	12.7±2.9	15.5±1.3	2.1±0.8	3.0±2.4	4.0±0.7
Model (%/100mmHg)	16.0	19.2	31.5	5.3	5.5	6.0
$\mathbf{C_{d,stat}}$(ID)						
Experiment (%/100mmHg)	13.0±2.4	12.9±7.8	16.4±4.6	1.3±1.2	2.5±3.3	4.1±4.9
Model (%/100mmHg)	16.9	20.3	33.9	5.5	5.8	6.2
$\mathbf{C_{d,stat}}$(OD)						
Experiment (%/100mmHg)	10.1±1.9	9.7±5.9	12.2±3.9	0.5±0.7	1.7±2.1	2.4±4.5
Model (%/100mmHg)	9.7	9.8	14.2	2.0	2.8	2.0

Figures

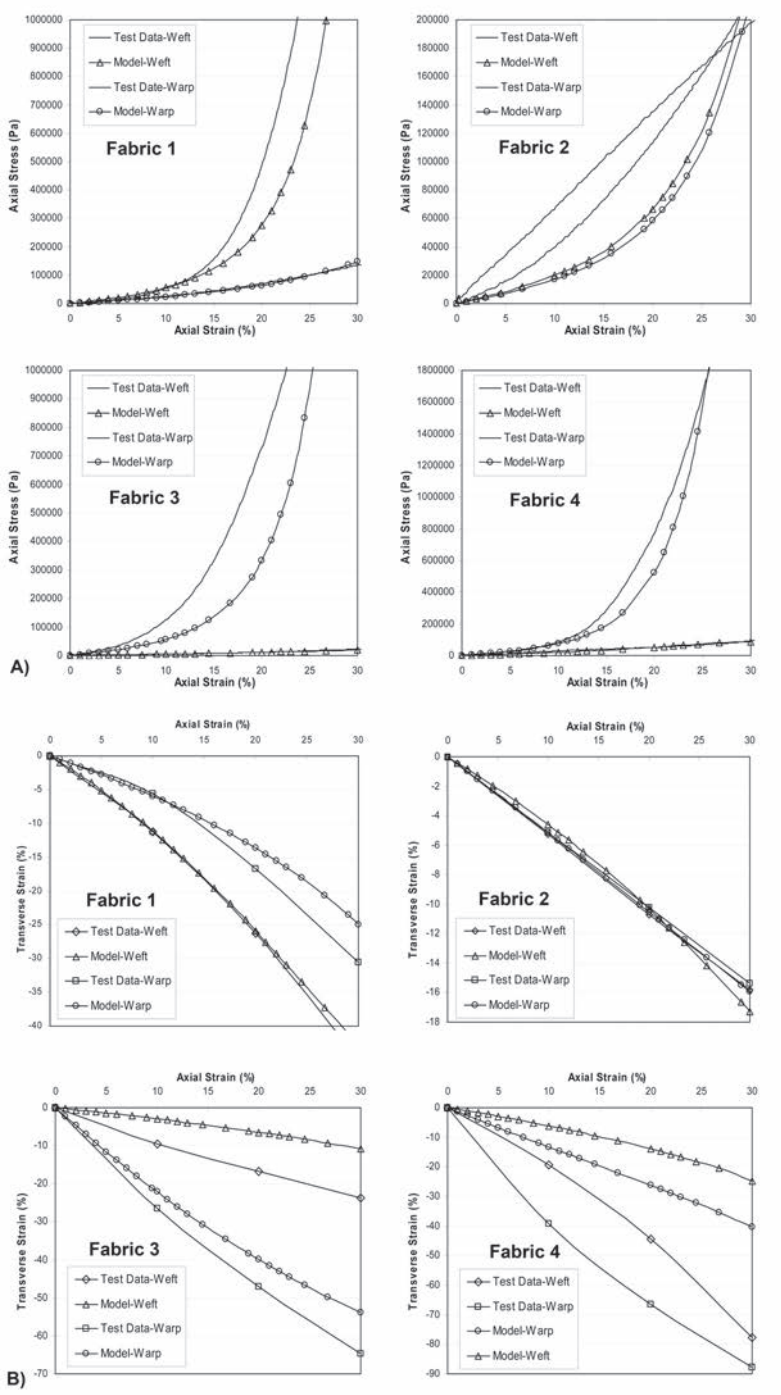

Figure 1: Comparison of experimental and numerical data of fabric tensile stress-strain behavior of four different fabrics: A) Uniaxial stress vs. strain, B) Transverse strain vs. axial (longitudinal) strain.

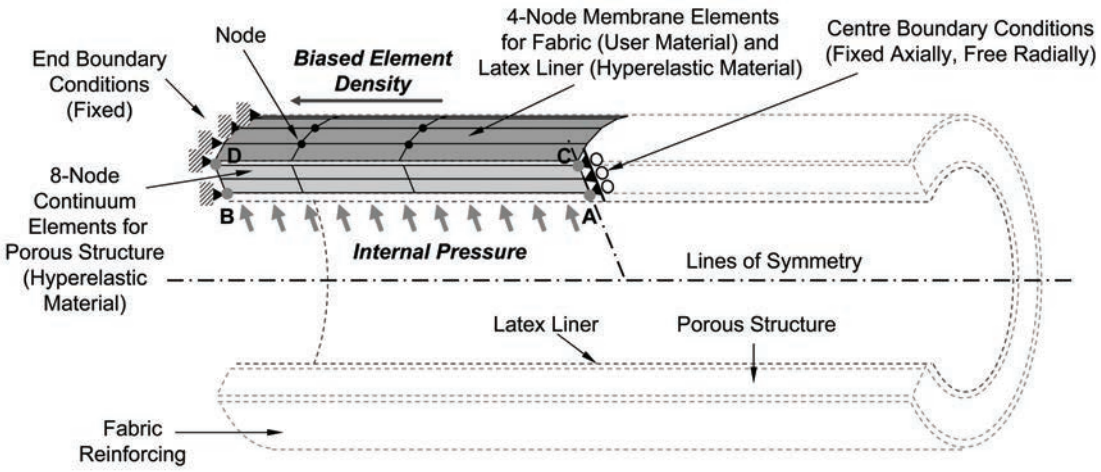

Figure 2: Graft finite element model.

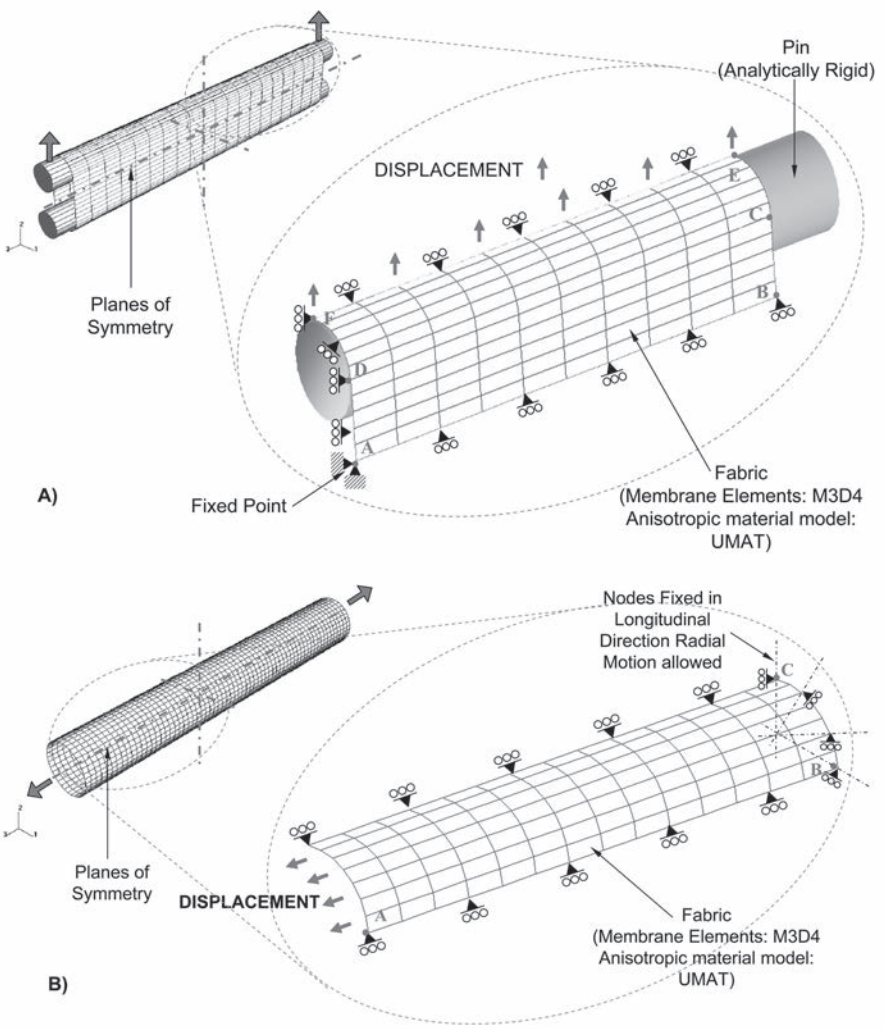

Figure 3: Quarter symmetric finite element mesh of the circumferential (A) and longitudinal (B) tensile test.

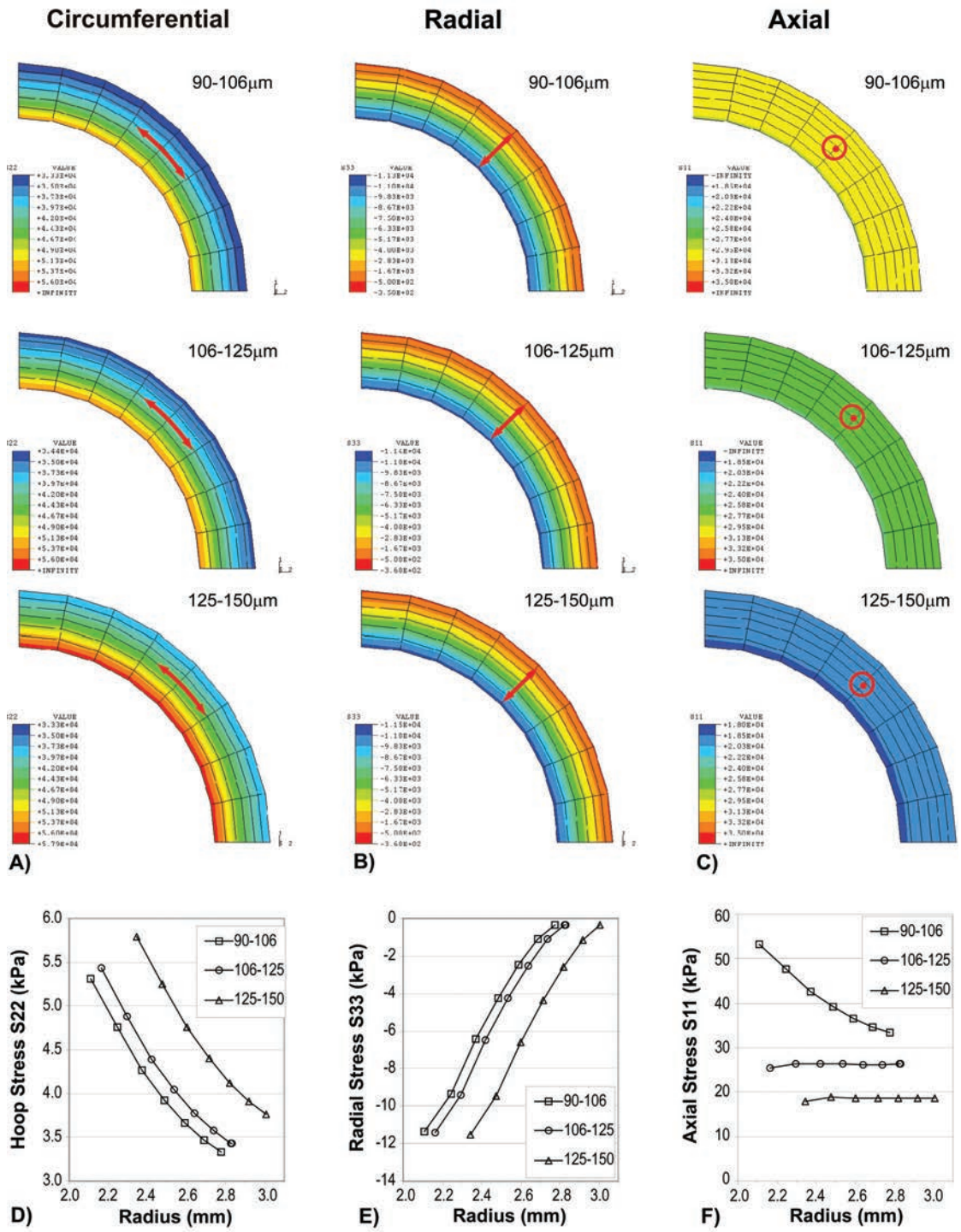

Figure 4: Contour plots and graphs showing the stress variation through the wall thickness of 90-106, 106-125 and 125-150 μm porous grafts at a luminal pressure of 100 mmHg: Circumferential stress (A, D), radial stress (B, E), axial stress (C, F).

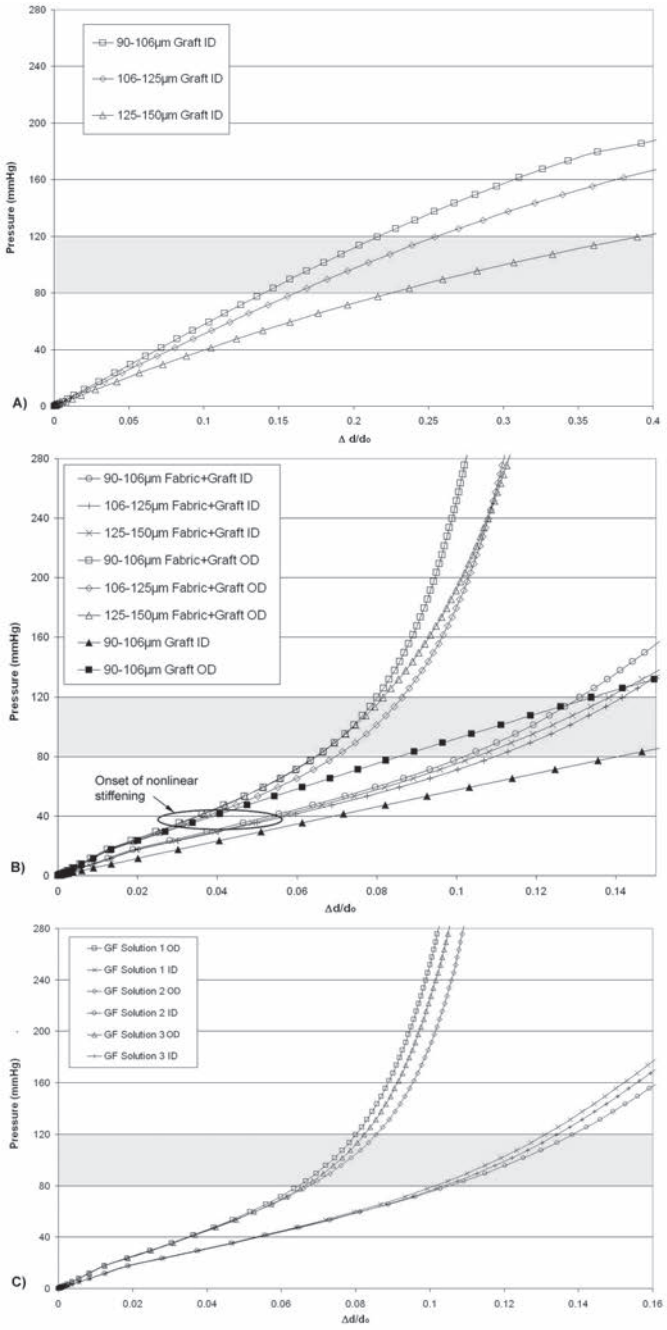

Figure 5: Numerical data of static pressure vs. change in internal (ID) and external (OD) diameter for the porous grafts of of 90-106, 106-125 and 125-150 μm porogen size: A) Change of ID of non-reinforced grafts. B) Change of ID and OD of optimally fabric reinforced grafts compared to non-reinforced graft with 90-106 μm porogen size. Fabric reinforcement solutions were obtained with the GA (see Table 2). C) Change of ID and OD for the three best fabric reinforced solutions obtained from genetic algorithm GA1 for the 125-150 μm graft (see Table 3).

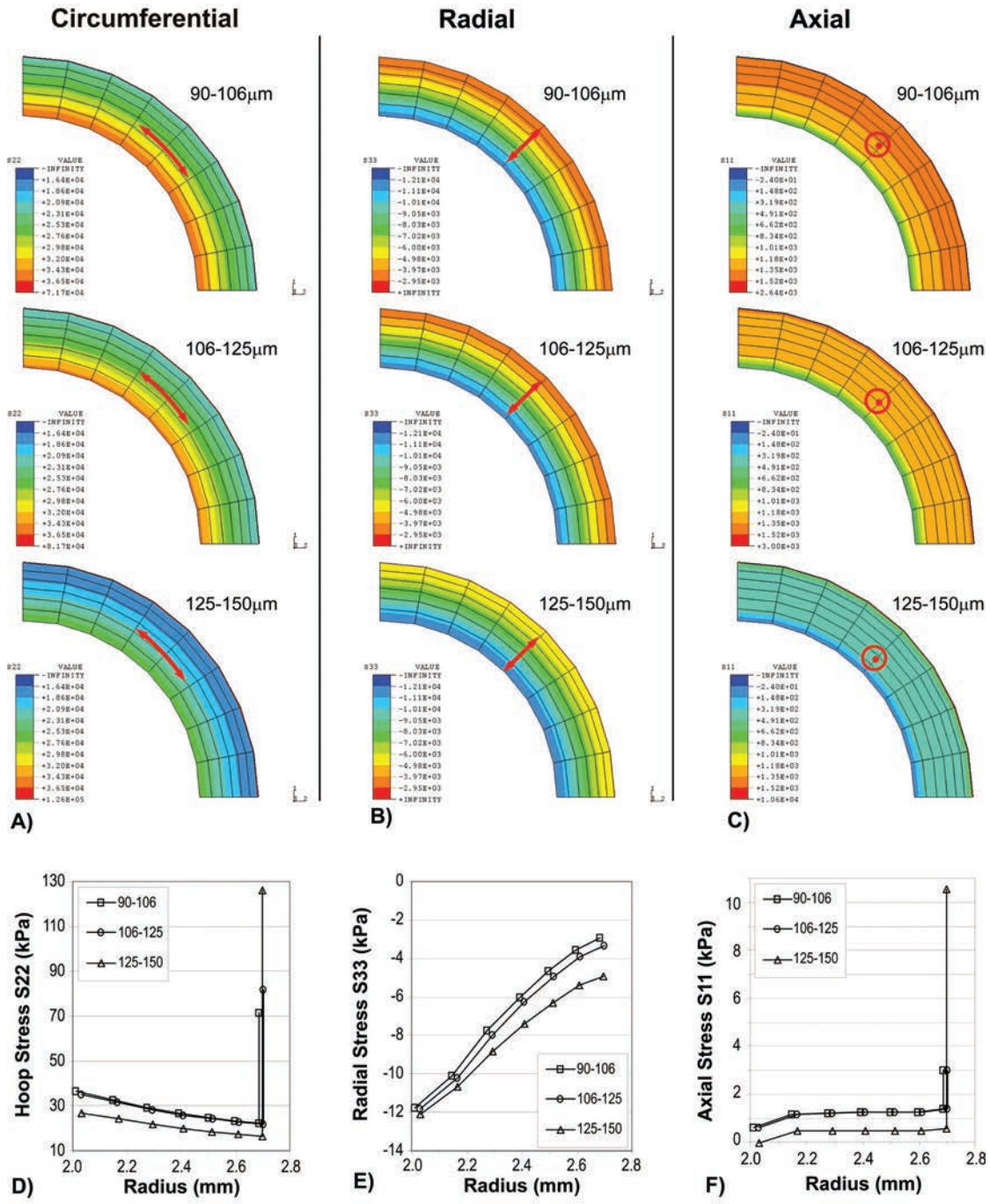

Figure 6: Contour plots and graphs showing the stress variation through the wall thickness of 90-106, 106-125 and 125-150 μm porous grafts with adventitial fabric reinforcement at a luminal pressure of 100 mmHg: Circumferential stress (A, D), radial stress (B, E), axial stress (C, F).

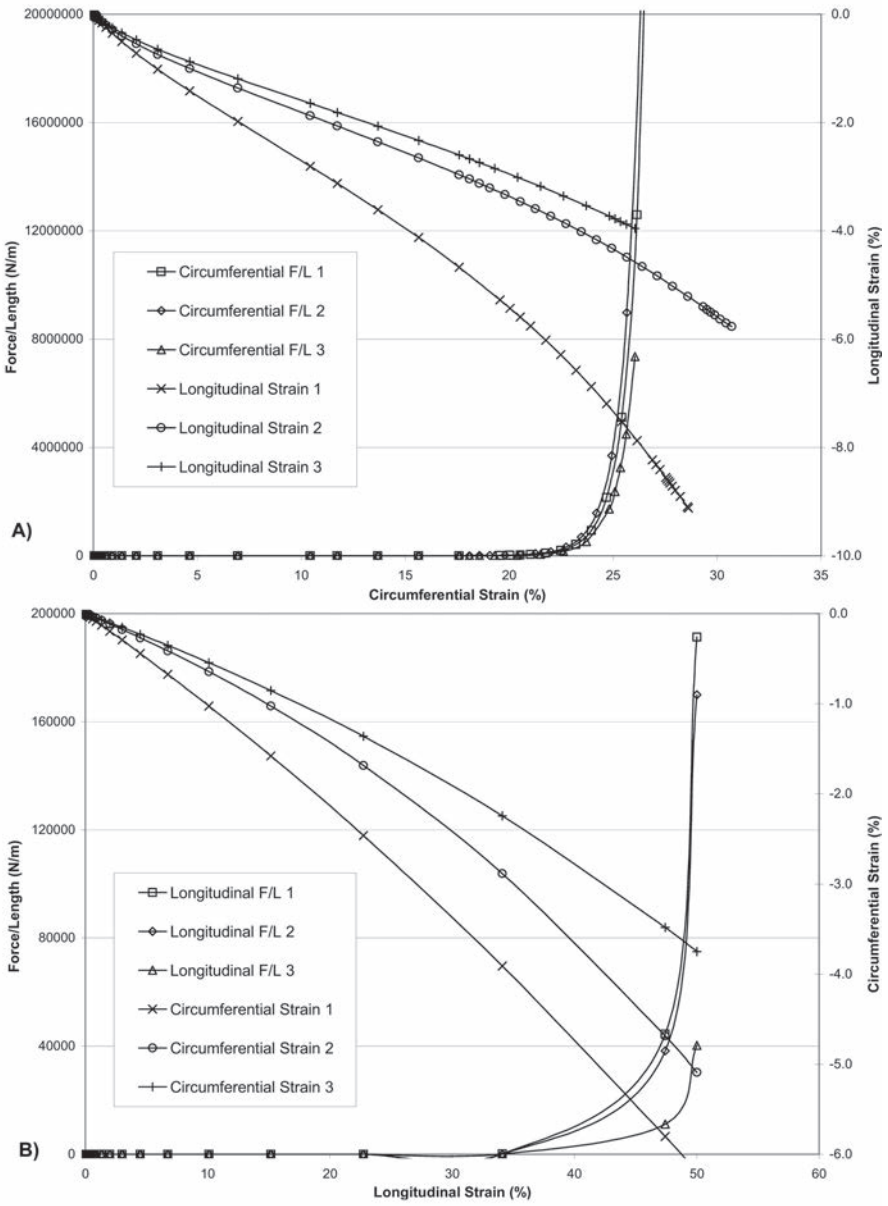

Figure 7: Numerical predicted force-strain interactions of the three best fabric reinforcing solutions for 125-150 μm porogen size grafts obtained from the GA: A) Normalized circumferential force and longitudinal strain vs circumferential strain obtained from numerical simulations of a circumferential tensile test, B) Normalized longitudinal force and circumferential strain vs longitudinal strain obtained from numerical simulations of a longitudinal tensile test.

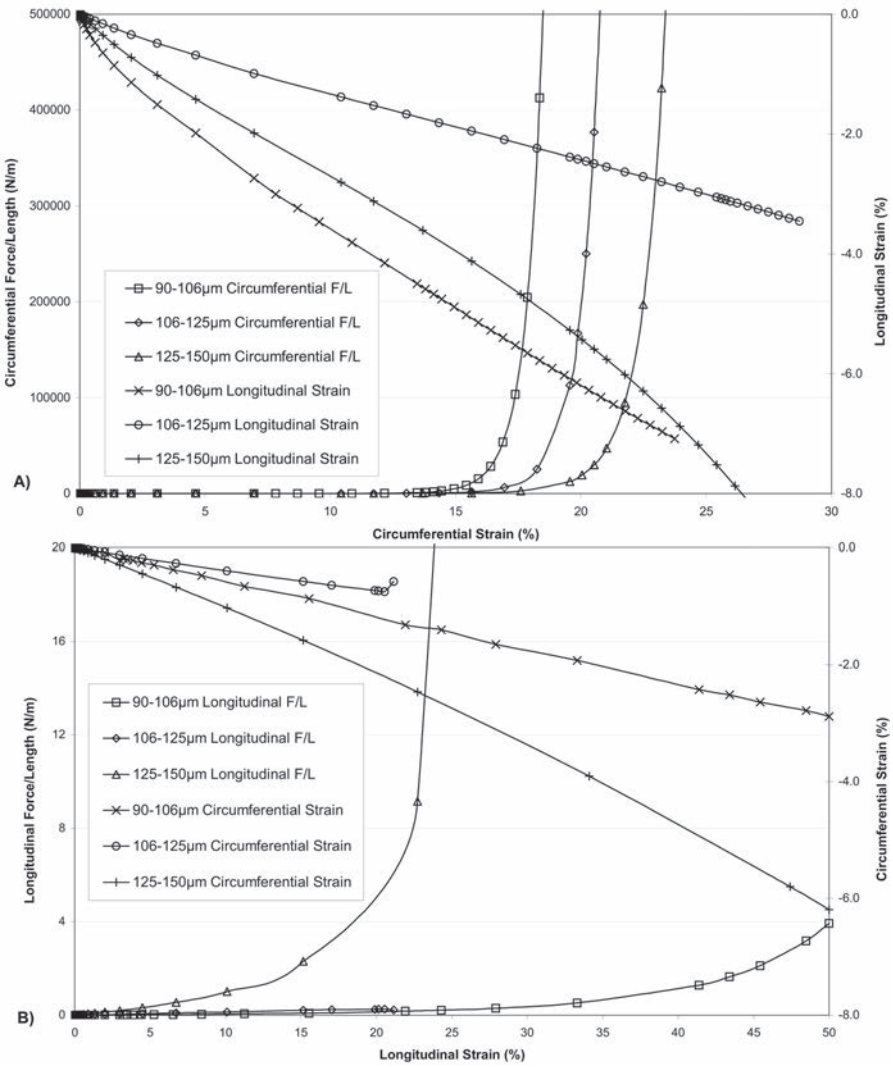

Figure 8: Numerical predicted force-strain interactions of the optimal reinforcing solution for 90-106, 106-125 and 125-150 μm porogen size grafts obtained from the GA (see Table 2): A) Normalized circumferential force and longitudinal strain vs circumferential strain obtained from numerical simulations of a circumferential tensile test, B) Normalized longitudinal force and circumferential strain vs longitudinal strain obtained from numerical simulations of a longitudinal tensile test.

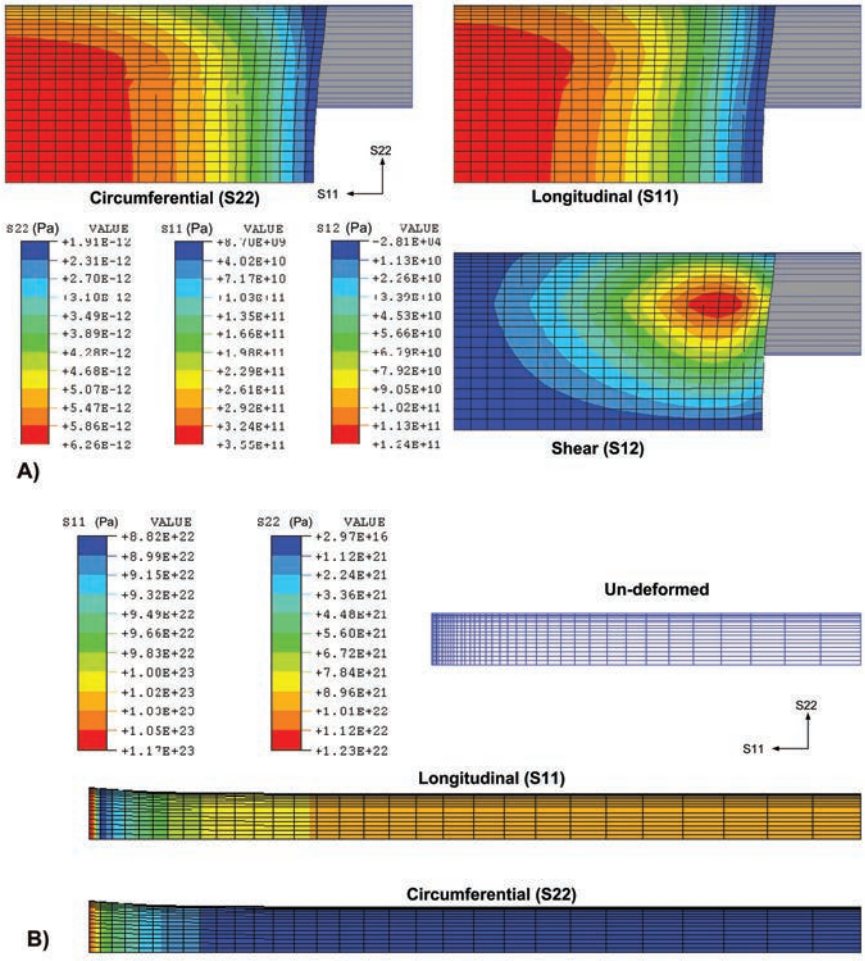

Figure 9: Stress distribution for optimal fabric-reinforced 125-150 μm porogen size graft: A) Circumferential ($S22$), axial ($S11$) and shear ($S12$) stress for circumferential tension, B) Circumferential ($S22$) and axial ($S11$) stress for longitudinal tension.

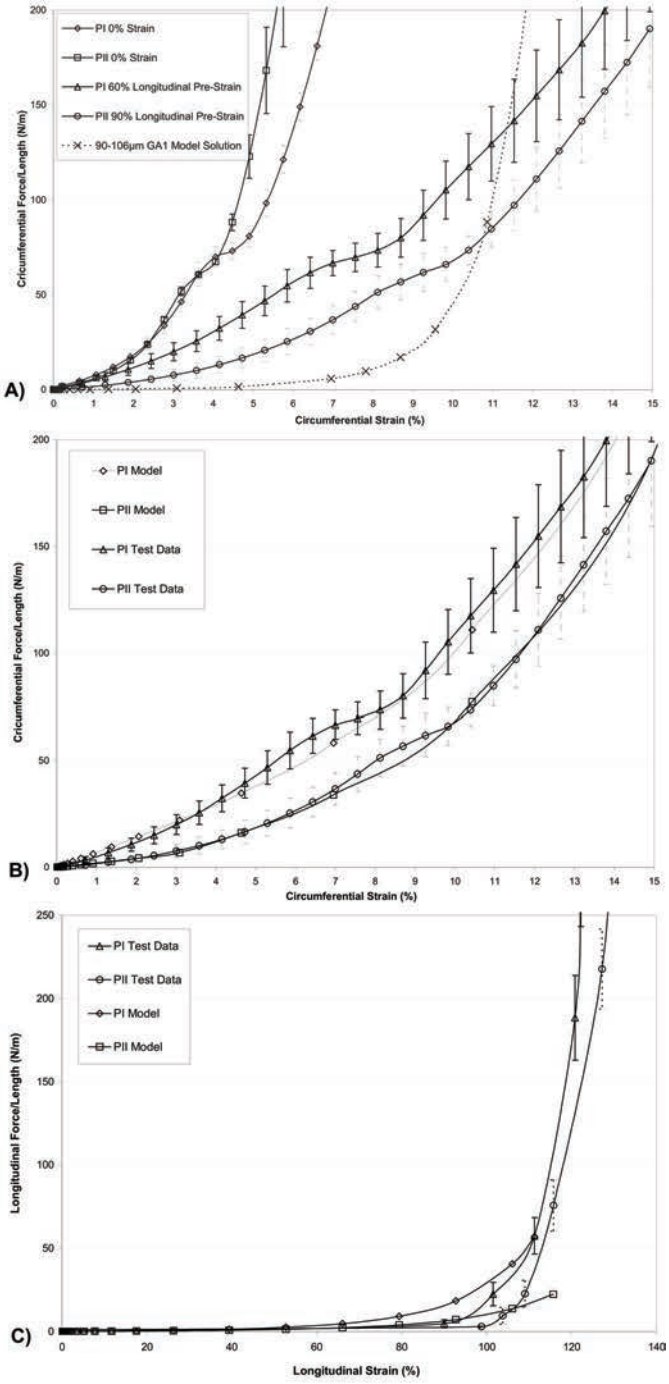

Figure 10: Experimental and numerical data for the final fabric sock prototypes I (PI) and II (PII): A) Force-displacement curves from circumferential tensile tests of the samples without and with longitudinal pre-strain and the optimal fabric model solution for 90-106 μm porogen size graft, B) Fabric model solutions and experimental data for circumferential tensile tests of pre-strained fabric samples, C) Fabric model solutions and experimental data for longitudinal tensile tests of pre-strained fabric samples.